Results in Physics 35 (2022) 105417

Contents lists available at ScienceDirect

Results in Physics

journal homepage: www.elsevier.com/locate/rinp

Realization of double Fano resonances with a InSb-doped Fabry-Perot cavity

Tao Zhang [a], Dan Zhang [b], Hai-Feng Zhang [a,*]

[a] *College of Electronic and Optical Engineering & College of Microelectronics, Nanjing University of Posts and Telecommunications, Nanjing 210023, China*
[b] *College of Information Science and Technology, Nanjing Forestry University, Nanjing 210037, China*

ARTICLE INFO

Keywords:
Fano resonance
Fabry-Perot cavity
Photonic crystals
InSb
Transfer matrix method

ABSTRACT

In this paper, a one-dimensional photonic structure is proposed for the realization of double Fano resonance (DFaR), which can be tuned by an external magnetic field and temperature. The designed photonic structure is composed of a Fabry-Perot cavity based on semiconductor material indium antimonide (InSb) and a sequence of general photonic crystals. A single Fano resonance (SFaR) is generated by the Fabry-Perot cavity, and the ordinary photonic crystals added to the back of the Fabry-Perot cavity offer a continuous transmission spectrum as a continuous state. The appearance of DFaR is ascribed to the interference phenomenon between SFaR and the continuous state. The effect of different parameters on Fano resonance was simulated by the transfer matrix method. The simulation results show that the interaction of the SFaR with the continuum spectrum leads to a new Fano resonance (NFaR) with a higher quality factor. Furthermore, DFaR can have the function of multi-physics tuning, controlled by the external magnetic field and temperature for the amplitude and frequency point of transmittance due to the introduction of InSb material. Based on the characteristics of DFaR, these obtained results can provide ideas for designing multi-measuring optical filters, lasers, slow light devices, and multi-node optical switches.

Introduction

The Fano resonance (FR) [1–3] is a special resonance generated by the mutual interference between broadband super-radiation mode (bright mode) and narrowband sub-radiation mode (dark mode). When there are two resonances in the structure at the same time, these two resonances may interfere with each other to produce an asymmetric linear FR. It can be said that the FR is a special new resonance generated by the combination of two resonance modes. For a long time, FR has been considered to exist only in quantum systems [4,5], and the FR phenomenon was observed for the first time in an optical system is Wood's anomaly [6]. After calculation, Wood's anomaly line type is completely consistent with the Fano formula, so it is the FR phenomenon in the optical system. The asymmetric line type of Fano profiles, different from the traditional symmetrical Lorentz resonance line type, has been researched widely and observed experimentally in many systems, including metamaterials [7–9], nanoclusters [10–12], photonic crystals (PCs) [13–15], and so on [16]. As is known to all, for highly integrated optical circuits, the array structure is usually too complex, bulky, and loss is inevitably large. Compared with other systems, the PCs naturally have the advantage of low loss, which is more suitable for the demands of large-scale integration in the future.

In the PCs, FR emerges from the interference between the broad continuum and the narrow discrete response of the physical system, and this process results in a sharp change in the reflection or transmission of the incident light in the PCs. Considering the characteristics of PCs, the photonic band gap is adopted as the continuous state, and the photonic local characteristic is served as the discrete state. Resonance with the shape of the Fano line will occur due to the coupling between the two at a specific frequency band. Gao *et al.* [17] investigated a structure constructed from three one-dimensional (1-D) PCs and a defect layer, and the experimental results demonstrated that the emerged FR can be attributed to the weak coupling between a Fabry-Perot cavity mode and a topological edge state mode provided by the topological PCs heterostructure. Because of its interference characteristics, FR has stronger scattering characteristics and field intensity enhancement ability than other symmetric line resonance. It is worth noting that the application of resonances generated in PCs makes it play an irreplaceable role in improving the performance of the sensors, such as quality factor and sensitivity, specifically in ultra-high sensitivity temperature sensors

* Corresponding author.
E-mail address: hanlor@163.com (H.-F. Zhang).

https://doi.org/10.1016/j.rinp.2022.105417
Received 16 January 2022; Received in revised form 25 February 2022; Accepted 9 March 2022
Available online 11 March 2022

[18–20], refractive index sensors [21–23], and biosensors [24–25]. Furthermore, it has important applications in optical instruments, such as optical filters [26–28], nonreciprocal propagation [29–31], and slow light devices [32–34].

In the last decade, the double Fano resonance (DFaR) [35–37] and even multi-Fano resonance [38,39] have become more and more significant and attracted the attention of researchers for the advantage of enhanced biosensing, and other optical equipment. In order to obtain the FR, a conventional method is to break the symmetry of the structure. Qi *et al.* [37] proposed an asymmetric metal-insulator-metal (MIM) waveguide structure consisting of a MIM waveguide and a rectangular cavity to support DFaR and investigated the cause of the formation of DFaR, which is derived from different mechanisms to achieve tunable properties for DFaR. Li *et al.* [39] extended the MIM structure and advanced the theory one step further on the basis of Qi *et al.* They explain the tunable triple Fano resonances in the modified MIM structure based on the multimode interference coupled mode theory, which provides a new direction for our understanding of the multi-Fano resonance.

The FR has been researched experimentally and verified theoretically by many approaches such as the quantum mechanical energy level model [40,41] which reveals the nature of the matter in the objective world, classically powerful and effective temporal coupled-mode theory [42,43], intuitive and distinctly understanding coupled oscillator model [44,45]. Considering the effect that the Fabry-Perot cavity can reflect and enhance the electromagnetic waves (EMWs) in the cavity several times, the Fabry-Perot cavity is mostly used for the existence and enhancement of FR [17,46]. In this paper, a 1-D photonic structure composed of Fabry-Perot cavity providing a strong trapped resonance for the emergence of the FR and common PCs is proposed to investigate FR due to the little research on DFaR in photonic structures and the low loss of PCs and their suitability for future large-scale integration. The DFaR in the proposed 1-D photonic structure is simulated by the transfer matrix method making an analogy with the triple coupled oscillator model [47,48] to reveal the principle of FR formation clearly. In the Fabry-Perot cavity, the semiconductor material InSb [49–51] is introduced as the defect layer to adjust the frequency point of FR in the terahertz (THz) range. Wang *et al.* [52] proposed a tunable THz filter based on InSb, and they found that the desired resonance frequency can be selected and tuned conveniently in the THz region, which highlights the excellent tuning of InSb in the THz region. The introduction of InSb in the proposed photonic structure provides an opportunity to tune the location of the FR point in the THz region. The tuning of DFaR based on the InSb-doped Fabry-Perot cavity is achieved, controlled by temperature T, magnetic field B. These calculation results can offer an approach for the realization of multi-frequency optical switches and high-performance sensors.

Structure design and simulation

The whole configuration of the proposed 1-D photonic structure with InSb is schematically displayed in Fig. 1. The proposed structure consists of a Fabry-Perot cavity (PC3) and the ordinary PCs (PC4) resting on the *xoz* plane. A and C represent ordinary dielectric layers. Fabry-Perot cavity adopted widely for promoting the formation of FR is made up of two conventional mediums alternately arranged with the refractive indices of $n_A = 3$, $n_C = 1$, whose lengths are $d_1 = 2$ μm, $d_2 = 2$ μm, and the semiconductor layer of InSb expressed as P layer with the thickness of $d_3 = 4$ μm. Moreover, PC4 as a continuous state forming a DFaR is composed of dielectric layer C with the length of $d_4 = 6.5$ μm, and D also denotes a common dielectric layer signified as a part of PC4 with the refractive index of $n_D = 2$ and its thickness is $d_5 = 6.5$ μm. Layers A, C, and D, which served as an isotropic medium, are not affected by temperature and magnetic field. In addition, the setting of the transverse magnetic (TM) wave and coordinate axis are illustrated in Fig. 1. TM wave enters the medium obliquely at an incident angle of θ, where the magnetic field is perpendicular to the *xoz* plane. The structure of the Fabry-Perot cavity is arranged in the order of "AC-P-CA", and the repeat number of "AC-AC" is $N_1 = 2$ with P layer adopted as a defect layer. Likewise, PC4 is composed of "DC" media and arranged in the form of "DC-DC" with the period number of $N_2 = 4$. The corresponding initial parameters for structure and external field are shown in Table 1.

As is known to all, the dielectric constant tensor ε_P of InSb is written as [53],

$$\boldsymbol{\varepsilon p} = \begin{bmatrix} \varepsilon x & 0 & \varepsilon xz \\ 0 & \varepsilon y & 0 \\ -\varepsilon xz & 0 & \varepsilon x \end{bmatrix} \tag{1}$$

$$\varepsilon_x = \varepsilon_\infty - \varepsilon_\infty \frac{\omega_p^2(\omega + j\nu_c)}{\omega\left[(\omega + j\nu_c)^2 - \omega_c^2\right]} \tag{2}$$

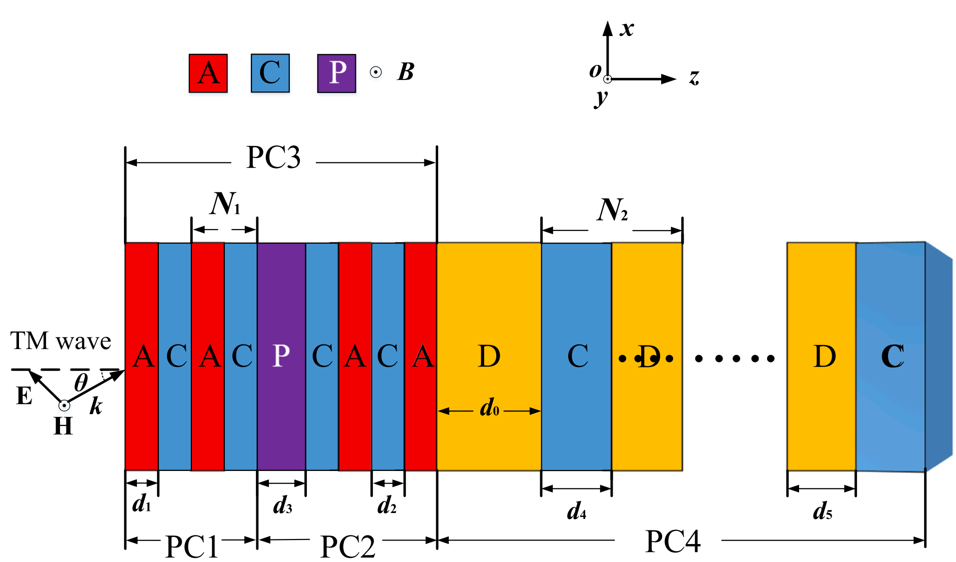

Fig. 1. The whole configuration of the proposed 1-D photonic structure composed of Fabry-Perot cavity including PC1 and PC2 and the ordinary PCs that produces the continuum of states.

Table 1
The initial parameters for structure and external field.

Object of the study	Parameters	
Structure	$d_1 = 2$ μm	$n_A = 3$
	$d_2 = 2$ μm	$n_C = 1$
	$d_4 = 6.5$ μm	$n_C = 1$
	$d_5(d_0) = 6.5$ μm	$n_D = 2$
	$d_3 = 4$ μm	
	$N_1 = 2$	
	$N_2 = 4$	
Incident angle	$\theta = 0^{\circ}$	
External field	$B = 0.8$ T	
	$T = 300$ K	

$$\varepsilon_y = \varepsilon_\infty - \varepsilon_\infty \frac{\omega_p^2}{\omega(\omega + j\nu_c)} \tag{3}$$

$$\varepsilon yz = \varepsilon_\infty \frac{j\omega_p^2\omega_c}{\omega[(\omega + j\nu_c)^2 - \omega_c^2]} \tag{4}$$

where the cyclotron frequency is $\omega_c = eB/m^*$. ν signifies the collision frequency of carriers with the expression: $\nu = e/(\mu_0 m^*) = 0.1\pi$ THz, where e is the electron charge, and m* is the effective mass of the carrier with the value of $m^*=0.015m_e$. ε_∞ is a coefficient in front of the equation, denoted the high-frequency limit permittivity, whose value is usually set to 15.68. ω is the circular frequency of the incident EMWs, and ω_P represents the plasma frequency[53],

$$\omega p = (N_{InSb}e^2/\varepsilon_0 m^*)^{1/2} \tag{5}$$

where N_{InSb} is intrinsic carrier density for InSb. ε_0 is the free-space permittivity. The expression of N_{InSb} is given by the following formula [53],

$$N_{InSb} = 5.76 \times 10^{20} T^{1.5} exp[-0.26/(2 \times 8.625 \times 10^{-5} \times T)] \tag{6}$$

In general, the dielectric tensor of InSb exhibits strong dispersion and gyrotropy characteristics, which depend to a large extent on the applied magnetic field and temperature in the THz region.

The transfer matrix for InSb can be written as [54],

$$\boldsymbol{M}_P = \begin{bmatrix} cos(k_z d_3) + \frac{k_x\varepsilon_{xz}}{k_z\varepsilon_x}sin(k_z d_3) & -\frac{j}{\eta_3}[1 + (\frac{k_x\varepsilon_{xz}}{k_z\varepsilon_x})^2]sin(k_z d_3) \\ -j\eta_3 sin(k_z d_3) & cos(k_z d_3) - \frac{k_x\varepsilon_{xz}}{k_z\varepsilon_x}sin(k_z d_3) \end{bmatrix} \tag{7}$$

where the expression of the optical admittance is $\eta_3 = n_3/\cos\theta$ for TM polarization, and n_3 signifies the effective refractive index of InSb. The inverse components of the wave vectors at x- and z-axis are $k_x = \omega n_3 \sin\theta/c$ and $k_z = \omega n_3\cos\theta/c$. c is the speed of light in a vacuum.

For common PCs, the transfer matrix can be represented as [54],

$$\boldsymbol{M}_{i=A,\ C,\ D} = \begin{bmatrix} \cos\delta_i & -\frac{j}{\eta_i}\sin\delta_i \\ -j\eta_i\sin\delta_i & \cos\delta_i \end{bmatrix} \tag{8}$$

where $\eta_i = n_i/\cos\theta_i$ for TM polarization, $\delta_i = \omega n_i d_i \cos\theta_i/c$, n_i indicates the refractive index of the layer *i*. d_i and θ_i signify the thickness and the incident angle of the layer *i*, respectively.

The field distribution which is attributed to dielectric layer *i* can be expressed as [54],

$$\begin{pmatrix} E_i \\ H_i \end{pmatrix} = \boldsymbol{M}\begin{pmatrix} E_{i+1} \\ H_{i+1} \end{pmatrix} \tag{9}$$

The transmission matrix of the whole configuration based on InSb with the sequence $(AC)^2P(CA)^2(DC)^4$ can be written as [54],

$$\boldsymbol{M} = \prod_{i=1}^{17}\boldsymbol{M}_i = \begin{pmatrix} M_{11} & M_{12} \\ M_{21} & M_{22} \end{pmatrix} \tag{10}$$

After deriving the matrix, the reflection coefficient *r* and transmission coefficient *t* can be given as [54],

$$r = \frac{(M_{11} + M_{12}\eta_0)\eta_0 - (M_{21} + M_{22}\eta_0)}{(M_{11} + M_{12}\eta_0)\eta_0 + (M_{21} + M_{22}\eta_0)} \tag{11}$$

$$t = \frac{2\eta_0}{(M_{11} + M_{12}\eta_0)\eta_0 + (M_{21} + M_{22}\eta_0)} \tag{12}$$

where $\eta_0 = n_0/\cos\theta_0$ for TM wave, n_0 stands for the refractive index of air. The transmittance $T_1(\omega)$ can be expressed as [54],

$$T_1(\omega) = |t|^2 \tag{13}$$

Where the reflectivity $R(\omega)=|r|^2$.

Analysis and discussion

Analysis of the formation mechanisms of SFaR and DFaR

To illustrate the generation mechanism of SFaR and DFaR clearly, the proposed structures are decomposed as PC3, made up of PC1 and PC2, and PC4, respectively. When the EMWs are incident separately, the appearance of asymmetric line patterns is judged from the observed changes in transmittance and the distribution of the electric field. Finally, a coupled harmonic oscillator model is used to analogize the proposed structure to illustrate the formation mechanism of the DFaR. As shown in Fig. 2(a and b), the Fabry-Perot cavity can form an asymmetric FR line pattern with a transmission peak of 0.94 and a corresponding frequency point of 10.25 THz, represented by a solid red line in Fig. 2(b). Through the separation of the Fabry-Perot cavity, the transmittance curves of PC1 and PC2 are obtained, as shown by the blue dashed line and the red solid line in the figure, respectively. Since the discrete state curve supported by PC2 is contained in the spectrum of the continuous state, an asymmetric resonance can be excited at the frequency of the discrete state. Especially, the proposed Fabry-Perot cavity conforms to the following phase formula [55],

$$\Phi = 2n\pi \tag{14}$$

where *n* takes an integer and Φ expresses the phase. Eq. (14) indicates the phase at the resonant frequency should be an integer multiple of 2π if the Fabry-Perot cavity is in resonance. As expected in Fig. 3, the phase is 0° (*n* takes 0) at the resonant frequency of 10.25 THz, and the transformation of phase is more obvious at the resonance frequency.

As displayed in Fig. 4, when the EMWs are incident into the Fabry-Perot cavity, the original electric field in PC1 and PC2 disappears locally, and an obvious electric field localization occurs on the A layer, which reveals that there is an appearance of new resonance in Fabry-Perot cavity. Since the proposed Fabry-Perot cavity satisfies the phase formula and makes the incident EMWs interfere multiple times in it, the Fabry-Perot cavity regarded as PC3 can provide an appearance of SFaR.

The triple coupled oscillator model is a good tool to intuitively and qualitatively explain the microscopic origins of DFaR, and the corresponding coupled oscillator model is shown in Fig. 5. A triple coupled oscillator model, motivated by external excitation *f*, can be described by the following set of differential equations of motion [47,48],

$$\begin{aligned} \ddot{x}_1 + \gamma_1\dot{x}_1 + \omega_1^2x_1 + g_1x_2 &= fe^{j\omega t} \\ \ddot{x}_2 + \gamma_2\dot{x}_2 + \omega_2^2x_2 + g_1x_1 + g_2x_3 &= 0 \\ \ddot{x}_3 + \gamma_3\dot{x}_3 + \omega_3^2x_3 + g_2x_2 &= 0 \end{aligned} \tag{15}$$

where γ_i ($i = 1, 2, 3$) expresses the frictional parameter, ω_i ($i = 1, 2, 3$) signifies the natural frequency (eigenmode) of each oscillator without

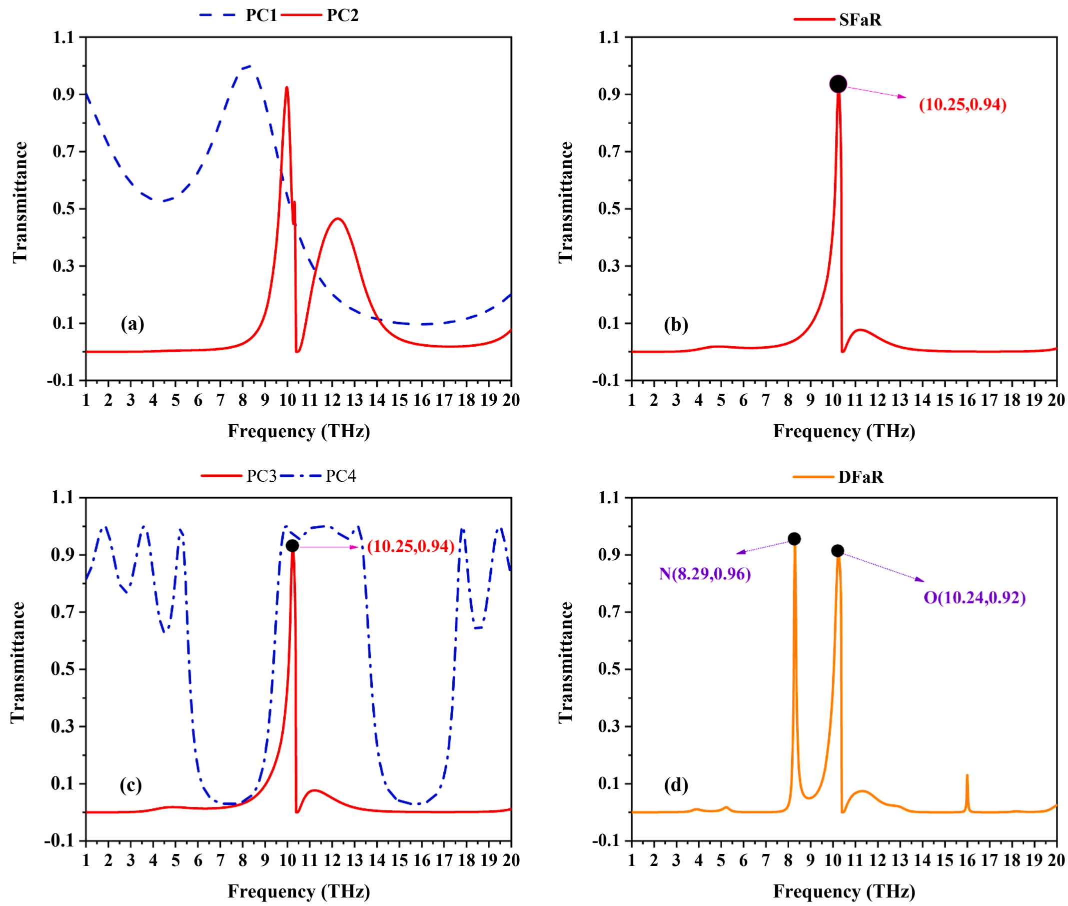

Fig. 2. Schematic diagrams of the transmittance of each part of the proposed structure. (a) The transmittance obtained when electromagnetic waves are incident on PC1 and PC2, respectively. (b) SFaR is produced by Fabry-Perot cavity. (c) SFaR is in the spectral range of a continuum state of PC4. (d) DFaR is formed by the combination of PC3 and PC4.

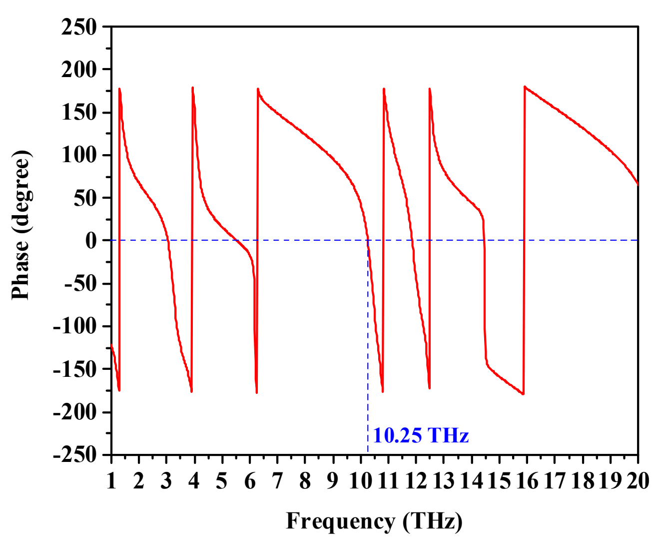

Fig. 3. The phase diagram of Fabry-Perot cavity served as PC3.

damping. The coupling strength between adjacent oscillators is determined by the spring constant g_i (i = 1, 2, 3), related to the coupled lengths d_3, and d_0. Each oscillator corresponds to PC1, PC2, PC4 respectively.

As portrayed in Fig. 5, PC1, as a continuous state, is able to act directly with the external forces (EMWs), and the transfer and exchange of energy with the outside materials take place in this process. As for PC2, which is taken as an excited narrow resonance in the Fabry-Perot cavity, it is able to interfere with the broad resonance to form an asymmetric transmission spectral line in the spectral range of the continuum state. Also, PC4 provides a wide resonance containing SFaR, so that the DFaR appears under the excitation of three different resonances. In DFaR, it is defined that the extreme point of the FR where SFaR is generated as original Fano resonance (OFaR) with the point of O, and the other asymmetry profile resembling that of FR is called as new Fano resonance (NFaR) with its extreme value as point N. It can be seen from Fig. 2(c and d) that a NFaR with N (8.29, 0.96) is achieved on the left of the point O (10.25, 0.92), and the extreme value of point O is smaller than that of SFaR, but the extreme value of the newly generated FR (point N) is larger than the two. Compared SFaR plotted with the red solid line with DFaR displayed by the orange solid line, superimposing a continuous transmission spectrum based on SFaR leads to a larger FR, and the extreme value at OFaR drops a little. According to the expression of quality factor, i.e. $f_0/\Delta f$, where f_0 signifies the center frequency, and Δf denotes the full width at half maxima. The quality factor of the SFaR in Fig. 2(b) is 29 from the expression of the quality factor, and the quality factor of the NFaR (quality factor = 65) is larger than that of the OFaR (quality factor = 28), which reveals that the interaction of the SFaR with the continuum spectrum results in a NFaR with the highest quality factor. From the above analysis, it is concluded that NFaR is easier to modulate than OFaR, and NFaR has a higher transmission efficiency.

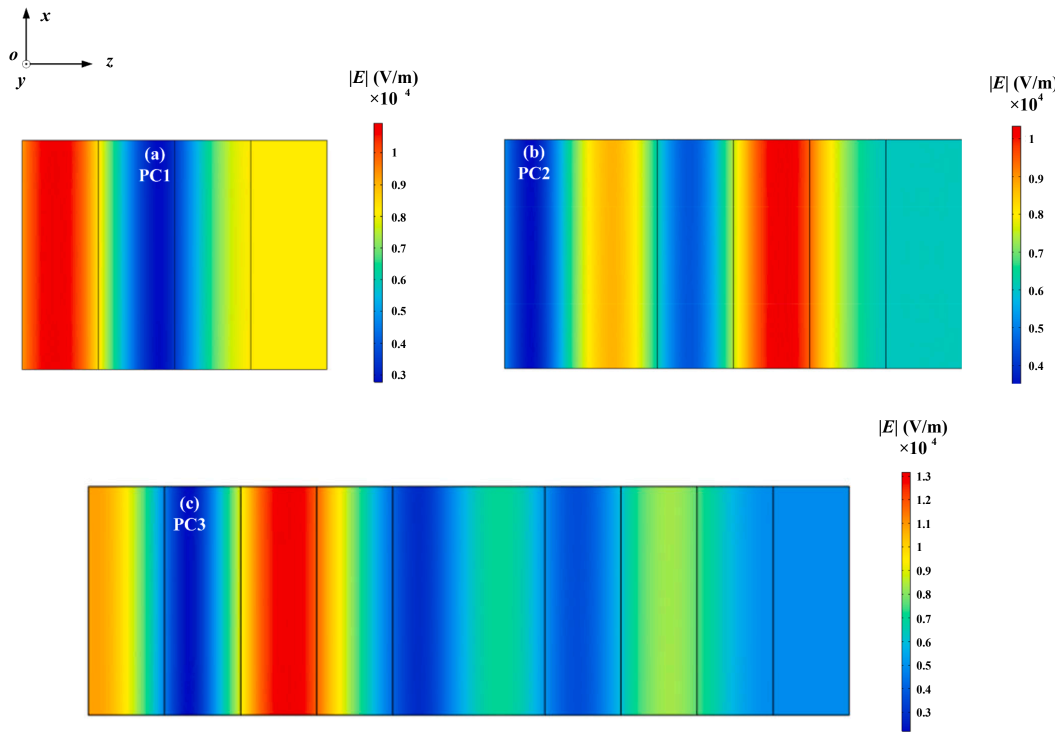

Fig. 4. The distribution of the electric field of the Fabry-Perot cavity. (a) PC1 at 10.25THz. (b) PC2 at 10.25THz. (c) at 10.25THz.

$$x_1 + \gamma_1 x_1 + \omega_1^2 x_1 + g_1 x_2 = f e^{j\omega t}$$
$$x_2 + \gamma_2 x_2 + \omega_2^2 x_2 + g_1 x_1 + g_2 x_3 = 0$$
$$x_3 + \gamma_3 x_3 + \omega_3^2 x_3 + g_2 x_2 = 0$$

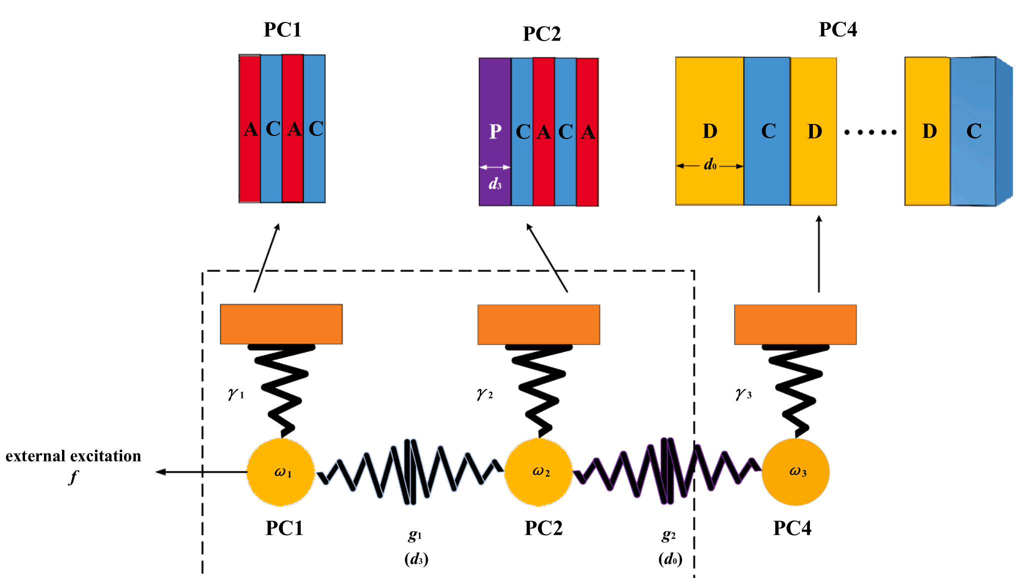

Fig. 5. Effective and intuitive mechanics model: triple coupled oscillators model, and corresponding photonic structures.

The effects of different parameters on the proposed structure

Before studying the DFaR generated by the proposed structure with different parameters, the length of the coupled layer needs to be investigated first to illustrate the effect of coupling distance on the FR. The diagrams of SFaR for the structure of PC3 with different d_3 are given in Fig. 6. Fig. 6(a and b) plot the transmittance curves of the Fabry-Perot cavity with different thicknesses of the coupled layer d_3, and its trajectory of the frequency point transformation at the maximum transmittance. As can be seen from the alteration of d_3, the transmission

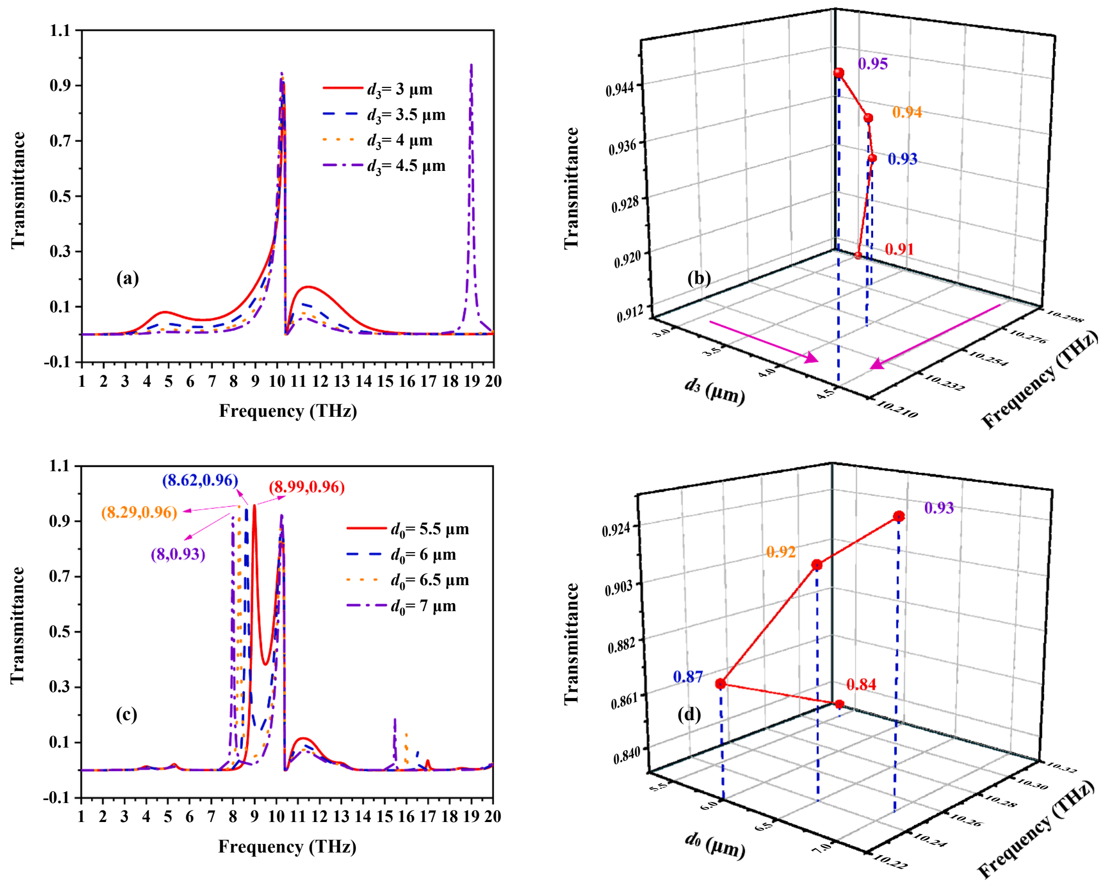

Fig. 6. (a) The transmittance curves of the Fabry-Perot cavity with different thicknesses of the coupled layer d_3, and (b) its trajectory of the frequency point transformation at the maximum transmittance. (c) The transmittance curves of the proposed structure with the variety of d_0, and (d) its trajectory of the frequency point transformation at the maximum transmittance.

curves shift towards low frequencies, and the peaks become stronger. Additionally, the transmittance peaks within the area of the OFaR get improved distinctly in Fig. 6(c and d). However, the peaks of the region of NFaR moves to the low frequency for meeting the phase-matching condition due to the amplification of the effective refractive index. It is worth noting that the OFaR changes very little, called independent tuning, while the NFaR gradually becomes a symmetric Lorentz type curve as it moves away from the SFaR, which can also be interpreted as the collapse of the FR caused by the weakening of the interaction between the SFaR and the continuum state provided by PC4 as the distance from the SFaR becomes farther away.

Next, since the variation of DFaR is influenced by SFaR, distinct parameters (B, T, and θ) are discussed on SFaR and DFaR below. Introducing PC4 as a continuous transmission spectrum, the original SFaR is associated with the interference of the continuous state, resulting in a more violent NFaR on the left side, thus forming DFaR. To present the impacts of B on SFaR and DFaR, the diagrams of their relationship for the proposed photonic structure with different B are given in Fig. 7. Fig. 7(a and b) show that the transmittance curves of the SFaR move to the lower frequencies with the increase of B. If $B = 0.4$ T, $B = 0.6$ T, $B = 0.8$ T, and $B = 1.0$ T, the maximum values of curves can reach 0.77, 0.89, 0.94, and 0.96 at the frequencies of 10.27 THz, 10.26 THz, 10.25 THz, and 10.22 THz, respectively. It is seen from formula $\omega_c = eB/m^*$ the variety of B can change the plasma cyclotron frequency ω_c, resulting in a transformation in the value of the transmittance, revealing that B can affect the SFaR. Moreover, it can also be considered that the extreme value changes precipitously and becomes larger as B rises with little shifts of extreme frequency point, which is favorable for the tuning of magnitude in optical facilities.

The diagrams of DFaR for the composite structure of PC3 and PC4 with different B are presented in Fig. 7(c). It can be seen that if $B = 0.4$ T, $B = 0.6$ T, $B = 0.8$ T, and $B = 1$ T, the coordinates of point N are (8.23, 0.89), (8.26, 0.92), (8.29, 0.96), (8.35, 0.97), respectively. Moreover, the point O can be found at 10.27 THz, 10.26 THz, 10.24 THz, and 10.22 THz, whose extreme values are 0.79, 0.88, 0.92, 0.94, respectively. DFaR can be tuned by changing T analogous to that of SFaR, while the effect on the OFaR is similar. The computed results also show that when B is strengthened, the extreme values of NFaR are enhanced. In addition, since the introduction of PC4, the NFaR is generated on the left side of the OFaR, and the extreme value of the NFaR is significantly larger than the OFaR. Not only a new FR but also a stronger FR can emerge in the whole system. The stronger FR results from the interference between the state of the OFaR and a new continuous transmission state. To better compare the difference between the OFaR and the NFaR, the rainbow diagram of DFaR with a continuous transformation of B from 0.1 T to 1.2 T is offered in Fig. 7(d). When B continuously increases, the maximum value of NFaR shifts to high frequencies, while the maximum values of OFaR move to the lower frequencies and are proportional to B. The area where NFaR is produced is significantly narrower than that of OFaR. In fact, the quality factor of NFaR is higher than that of OFaR. Generally speaking, the effect of B can enhance the transmittance of NFaR and OFaR, and the generation of NFaR with a higher quality factor.

The diagram of SFaR for the structure of PC3 with different T is given in Fig. 8(a). The transmittance curves of the SFaR move to the higher frequencies as the increase of T. When $T = 295$ K, $T = 300$ K, $T = 305$ K, and $T = 310$ K, the maximum values of the SFaR can arrive at 0.97, 0.94, 0.84, and 0.64 at the frequencies of 9.57 THz, 10.25 THz, 10.88 THz,

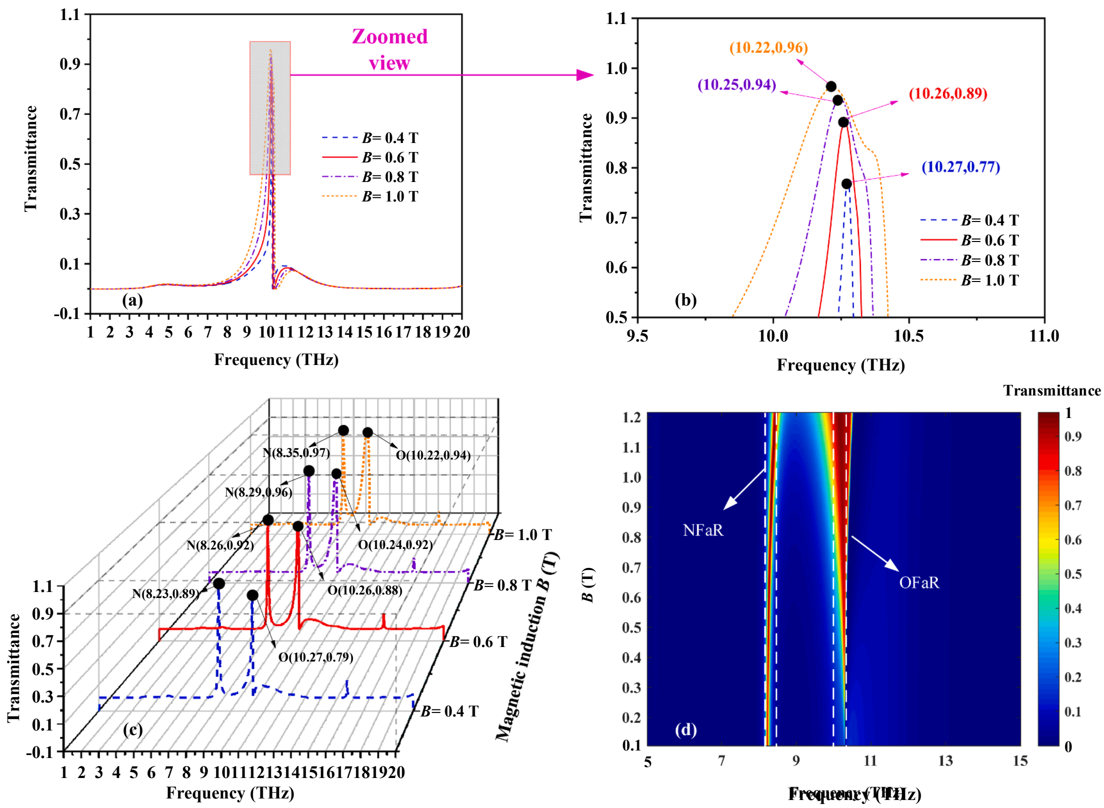

Fig. 7. (a) The diagram of SFaR for the structure of PC3 with different *B*, and (b) the zoomed view of the extreme values of the FR. (c) The diagrams of DFaR for the composite structure of PC3 and PC4 with different *B*. (d) The rainbow diagram of DFaR with different *B* ranging from 0.1 T to 1.2 T.

and 11.47 THz, respectively, which reveals that changing *T* can result in the shifts of SFaR. It can be seen from Eqs. (6) and (5) that changing *T* will affect the intrinsic carrier density N_{InSb}, then, the variety of N_{InSb} makes a difference in plasma frequency ω_p. There is no doubt that the transformation of *T* can indirectly affect ω_p, and the variety of *T* is the main factor that causes the movement of SFaR. In general, the effect of the temperature can make it play an irreplaceable role in SFaR. Fig. 8(b) shows that the curve of SFaR tends to move to high frequencies as *T* increases continuously, indicating that the transmittance value at the extreme value declines and the position of FR can be tuned over a certain frequency range by the varying temperature of InSb, which is consistent with the analysis result above. The maximum of SFaR at 9.57 THz for $T = 295$ K shifts to 11.47 THz for $T = 310$ THz with an increase in the temperature.

Similar to studying the effects of *T* on SFaR, the influences of *T* on DFaR are explored by changing *T* depicted in Fig. 8(c and d). As is shown in Fig. 8(c), when $T = 295$ K, $T = 300$ K, $T = 305$ K, and $T = 310$ K, the maximum of NFaR can reach 0.79, 0.96, 0.70, 0.41, which expresses the values of NFaR grow first, then decrease, analogous to the OFaR. The coordinates of point O are (9.78, 0.77), (10.24, 0.92), (10.87, 0.86), (11.47, 0.64), respectively. NFaR shifts from 8.65 THz to 8.06 THz, and OFaR develops from 9.78 THz to 11.47 THz. Moreover, the maximum of not only the NFaR but also the OFaR is optimal at $T = 300$ K. It is worth noting that as OFaR and NFaR gradually move away from each other, the asymmetric line shape of NFaR slowly diminishes until it degenerates into a Lorentz type curve due to the weakening of the coupling between OFaR and NFaR. By changing the values of *T*, DFaR can move left and right in the corresponding frequency band, which broadens the range of tuning range of DFaR, which facilitates the expansion of the tunability for the optical devices.

Finally, the changes of SFaR and DFaR to the angle of incidence are shown in Fig. 9. The simulation results exhibit that the variety of θ also plays a distinct role in SFaR and DFaR. As displayed in Fig. 9(a), when $\theta = 0^\circ$, $\theta = 20^\circ$, $\theta = 40^\circ$, $\theta = 60^\circ$, the maximum of SFaR reaches 0.94, 0.88, 0.79, 0.87, respectively. As θ increases, the maximum values of the FR first decrease and then become larger. When $\theta = 40^\circ$, the shape of the SFaR changes significantly. This phenomenon can be explained that the loss of incident electromagnetic wave in the medium rises with the increase of θ and the transmittance is not as large as that of $\theta = 0^\circ$. As plotted in Fig. 9(b), NFaR can appear normal with $\theta = 0^\circ$ and $\theta = 20^\circ$, and the coordinates of NFaR are (8.29, 0.96), (8.58, 0.97), respectively. However, there is the only appearance of SFaR if $\theta = 40^\circ$ and $\theta = 60^\circ$ with the extreme value of 0.63, and 0.80 at the frequency of 10.27 THz, and 10.28 THz, respectively. When θ increases, NFaR will disappear, and the DFaR will degenerate into SFaR, which exhibiting the appearance of DFaR is sensitive to the angle. This can be explained by the reason that the decrease in quality factor resulting from the reduced transmittance of the SFaR and the larger linewidth, leading to a lower probability of DFaR.

Conclusion

In summary, a 1-D photonic structure consisting of a Fabry-Perot cavity based on InSb and common PCs is applied to achieve the realization of DFaR. The effects of the properties for InSb (*B*, *T*), structure parameters, and incident angle on SFaR and DFaR are investigated, respectively. Changes in the magnetic field will cause transformation in the extreme values of SFaR and DFaR, and a variety of *T* will lead to the movement of frequency points, where NFaR evolves from 8.65 THz to 8.06 THz, and the frequency points of OFaR transfer from 9.78 THz to 11.47 THz. Moreover, it is observed that the quality factor of NFaR is larger than that of OFaR, which provides more favorable tuning for the NFaR. The simulation shows that DFaR is very sensitive to the change of incident angle. When the incident angle exceeds 40°, the DFaR disappears and evolves into SFaR, which can be explained by the weakening of the coupling between SFaR and DFaR due to the increase of the incident angle leading to the decrease of the quality factor. The proposed structure based on the tunability of magnetic field and

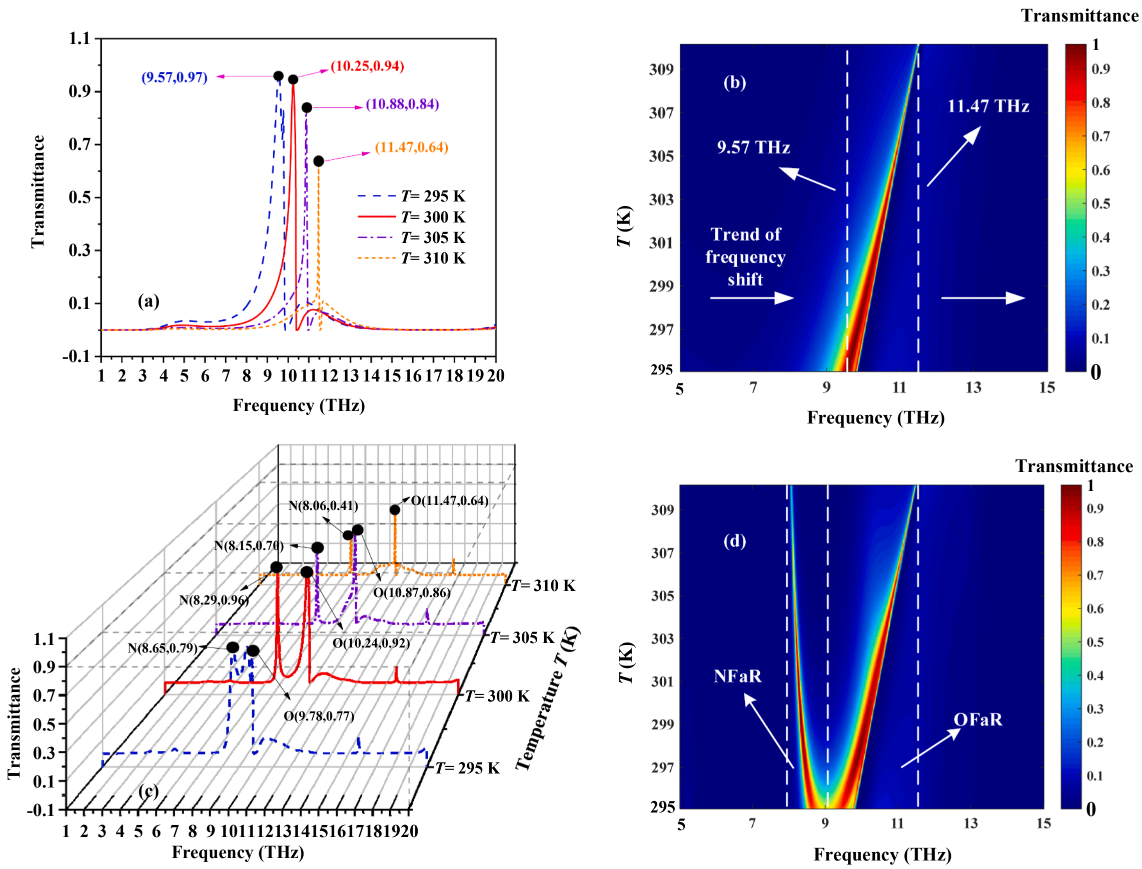

Fig. 8. (a) The diagram of SFaR for the structure of PC3 with different T. (b) The rainbow diagram of SFaR with continuous change of temperature T from 295 K to 310 K. (c) The diagrams of DFaR for the composite structure of PC3 and PC4 with different T. (d) The rainbow diagram of DFaR with different T from 295 K to 310 K.

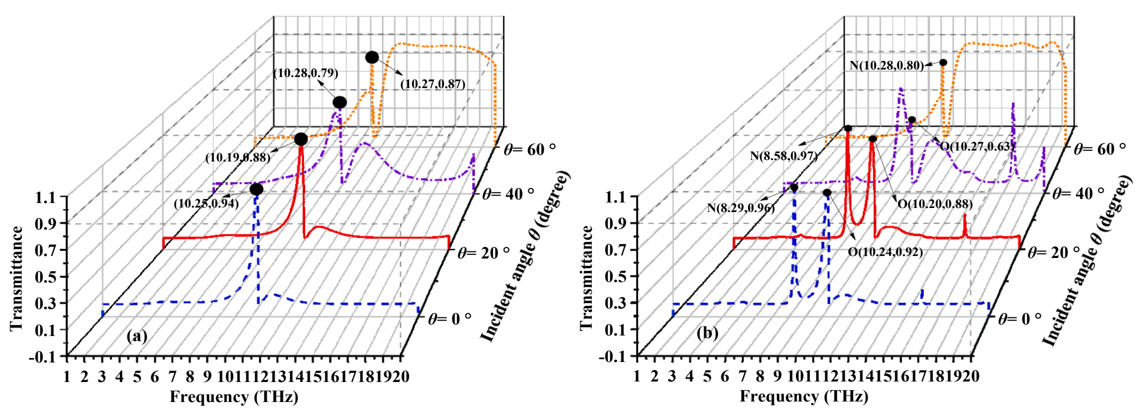

Fig. 9. (a) The diagram of SFaR for the structure of PC3 with different θ. (b) The diagrams of DFaR for the composite structure of PC3 and PC4 with different θ.

temperature of InSb can offer potential applications for multi-measuring optical filters, lasers, slow light devices, and multi-node optical switches.

Declaration of Competing Interest

The authors declare that they have no known competing financial interests or personal relationships that could have appeared to influence the work reported in this paper.

Acknowledgements

This work was supported by the Jiangsu Agriculture Science and Technology Innovation Fund (JASTIF) (Grant No. CX(21)3187), and the Open Research Program in China's State Key Laboratory of Millimeter Waves (Grant No. K201927).

References

[1] Wen Y, Chen KL, Lin YS. Terahertz metamaterial resonator with tunable Fano-resonance characteristic. Results Phys 2021;23:104049.
[2] Miroshnichenko AE, Flach S, Kivshar YS. Fano resonances in nanoscale structures. Review of Modern Physics 2009;82(3):2257–98.
[3] Zhang M, Zhang FL, Li M, Li P, Li JT, Li J, et al. Highly Efficient Amplitude Modulation of Terahertz Fano Resonance Based on Si Photoactive Substrate by Low Power Continuous Wave. Advanced Materials Technologies 2020;5:2000626.

[4] Fano U. Sullo spettro di assorbimento dei gas nobili presso il limite dello spettro d'arco. Il Nuovo Cimento 1935;12:154–61.
[5] Fano U. Effects of Configuration Interaction on Intensities and Phase Shifts. Phys Rev 1961;124:1866.
[6] A. Hessel A, and A. A. Oliner,. A New Theory of Wood's Anomalies on Optical Gratings. Appl Opt 1965;4(10):1275–97.
[7] Singh R, Al-Naib I, Cao W, Rockstuhl C, Koch M, Zhang WL. The Fano Resonance in Symmetry Broken Terahertz Metamaterials. IEEE Trans Terahertz Sci Technol 2013;3(6):820–6.
[8] Mun S, Yun H, Choi C, Kim S, Lee B. "Enhancement and Switching of Fano Resonance in Metamaterial", Advanced. Opt Mater 2018;6(17):1800545.
[9] Xu J, Fu QH, Fan YC, Nan JM, Zhang FL. Thermally Reconfigurable Fano Resonance in Water Brick Pair Metamaterial. Results Phys 2021;28:104650.
[10] Chen T, Xiang TY, Wang JW, Lei T, Lu FS. Double E-shaped toroidal metasurface with high Q-factor Fano resonance and electromagnetically induced transparency. AIP Adv 2021;11:095011.
[11] Du MY, Shen Z. Enhanced and tunable double Fano resonances in plasmonic metasurfaces with nanoring dimers. J Phys D Appl Phys 2021;54:145106.
[12] Liu ZH, Ye J. Highly controllable double Fano resonances in plasmonic metasurfaces. Nanoscale 2016;8:17665–74.
[13] Markoš P, Kuzmiak V. Coupling between Fano and Bragg bands in the photonic band structure of two-dimensional metallic photonic structures. Phys Rev A 2016; 94:033845.
[14] Mehaney A, Abadla MM, Elsayed HA. 1D porous silicon photonic crystals comprising Tamm/Fano resonance as high performing optical sensors. J Mol Liq 2020;322(7):114978.
[15] Mohamed AM, Sabra W, Aly AH, Mobarak M, Shalaby AS. A defective one-dimensional superconducting photonic crystal design for the generation of the Fano resonance feature. Phys Scr 2020;95:115503.
[16] Cao GT, Dong SH, Zhou LM, Zhang Q, Deng Y, Wang C, et al. Fano Resonance in Artificial Photonic Molecules. Adv Opt Mater 2020;1902153.
[17] Gao W, Hu XY, Li C, Yang JH, Chai Z, Xie JY, et al. Fano-resonance in one-dimensional topological photonic crystal heterostructure. Opt Express 2018;26(7): 8634–44.
[18] Zhu J, Lou J. High-sensitivity Fano Resonance Temperature Sensor in MIM Waveguides Coupled with a Polydimethylsiloxane-sealed Semi-square Ring Resonator. Results Phys 2020;18:103183.
[19] Ahmed AM, Mehaney A. Novel design of wide temperature ranges sensor based on Tamm state in a pyroelectric photonic crystal with high sensitivity. Physica E 2021; 125:114387.
[20] Ahmed AM, Elsayed HA, Mehaney A. High-performance temperature sensor based on one-dimensional pyroelectric photonic crystals comprising Tamm/Fano Resonances. Plasmonics 2021;16(23).
[21] Chen Y, Zhou XD, Zhang M, Xiao CY, Ding ZX, Zhou J. Fano resonance sensing based on coupled sub-wavelength dielectric grating and periodic photonic crystal. Phys Lett A 2020;384(34):126877.
[22] Ahmed AM, Mehaney A. Ultra-high sensitive 1D porous silicon photonic crystal sensor based on the coupling of Tamm/Fano resonances in the mid-infrared region. Sci Rep 2019;9:9673.
[23] Sagor RH, Hassan MF, Yaseer AA, Surid E, Ahmed MI. Highly sensitive refractive index sensor optimized for blood group sensing utilizing the Fano resonance. Applied Nanoscience 2020;11:521–34.
[24] Ruan BX, You Q, Zhu JQ, Wu LM, Guo J, Dai XY, et al. Fano resonance in double waveguides with graphene for ultrasensitive biosensor. Opt Express 2018;26(13): 16884.
[25] Mehaney A, Alrowaili ZA, Elsayed HA, Taha TA, Ahmed AM. Theoretical investigations of Tamm plasmon resonance for monitoring of isoprene traces in the exhaled breath: Towards chronic liver fibrosis disease biomarkers. Phys Lett A 2021;413:127610.
[26] Li X, Shen C, Yu XH, Zhang YQ, Chen C, Zhang XX. Bandwidth-tunable optical filter based on microring resonator and MZI with Fano resonance. J Opt 2020;49: 427–32.
[27] Shuai YC, Zhao DY, Tian ZB, Seo J, Plant DV, Ma ZQ, et al. Double-layer Fano resonance photonic crystal filters. Opt Express 2013;21(21):24582–9.
[28] Zhao WY, Leng XD, Jiang YY. Fano resonance in all-dielectric binary nanodisk array realizing optical filter with efficient linewidth tuning. Opt Express 2015;23 (5):6858–66.
[29] Ding W, Luk'yanchuk B, Qiu CW. Ultrahigh-contrast-ratio silicon Fano diode. Phys Rev A 2012;85:025806.
[30] Yu Y, Chen YH, Hu H, Xue WQ, Yvind K, Mork J. Nonreciprocal transmission in a nonlinear photonic-crystal Fano structure with broken symmetry. Laser Photonics Rev 2015;9(2):241–7.
[31] Wang XB, Zhang GQ, Li HH, Zhou J. Magnetically tunable Fano resonance with enhanced nonreciprocity in a ferrite-dielectric metamolecule. Appl Phys Lett 2018; 112(17):174103.
[32] Wang XY, Si LG, Lu XH, Wu Y. Optomechanically tuned Fano resonance and slow light in a quadratically coupled optomechanical system with membranes. J Phys B: At Mol Opt Phys 2020;53(23):235402.
[33] Yang MS, Song XX, Zhang HT, Ye YX, Ren YP, Ren XD, et al. Position-guided Fano resonance and amending GausssAmp model for control slow light in hybrid graphene-silicon metamaterials. Opt Express 2020;28(8):11933–45.
[34] Wei BZ, Jian SS. Fano resonance in a U-shaped tunnel assisted graphene-based nanoring resonator waveguide system. Opt Commun 2018;425:24–8.
[35] Artar A, Yanik AA, Altug H. Directional Double Fano Resonances in Plasmonic Hetero-Oligomers. Nano Lett 2011;11(9):3694–700.
[36] Yin LY, Huang YH, Wang X, Ning ST, Liu SD. Double Fano resonances in nanoring cavity dimers: The effect of plasmon hybridization between dark subradiant modes. AIP Adv 2014;4:077113.
[37] Qi JW, Chen ZQ, Chen J, Li YD, Qiang W, Xu JJ, et al. Independently tunable double Fano resonances in asymmetric MIM waveguide structure. Opt Express 2014;22(12):14688–95.
[38] Li H, Yu SL, Yang L, Zhao TG. High Q-factor multi-Fano resonances in all-dielectric double square hollow metamaterials. Opt Laser Technol 2021;140:107072.
[39] Li SL, Zhang YY, Song XK, Wang YL, Yu L. Tunable triple Fano resonances based on multimode interference in coupled plasmonic resonator system. Opt Express 2016; 24(14):15351–61.
[40] Chen J, Hu GW, Cao GT, Deng Y, Zhou LM, Wen ZJ, et al. Manipulating mode degeneracy for tunable spectral characteristics in multi-microcavity photonic molecules. Opt Express 2021;29(7):11181–93.
[41] Wang T, Hu YQ, Du CG, Long GL. Multiple EIT and EIA in optical microresonators. Opt Express 2019;27(5):7344–53.
[42] Fan SH, Suh W. Temporal coupled-mode theory for the Fano resonance in optical resonators. Journal of the Optical Society of America A 2003;20(3):569–72.
[43] Zhao X, Cheng Z, Zhu M, Huang TY, Zeng SW, Pan JX, et al. Study on the dual-Fano resonance generation and its potential for self-calibrated sensing. Opt Express 2020;28(16):23703–16.
[44] Joe YS, Satanin AM, Kim CS. Classical analogy of Fano resonances. Phys Scr 2006; 74:259–66.
[45] Gallinet B, Martin OJF. Ab initio theory of Fano resonances in plasmonic nanostructures and metamaterials. Physical Review B 2011;83:235427.
[46] Chen YH, Chen L, Wen KH, Hu YH, Lin WT. Double Fano resonances based on different mechanisms in a MIM plasmonic system. Photonic Nanostruct 2019;36: 100714.
[47] Lee YU, Choi EY, Kim ES, Woo JH, Kang B, Kim J, et al. Double Fano resonances in a composite metamaterial possessing tripod plasmonic resonances. J Opt 2015;17: 025103.
[48] Zhu XC, Cao N, Thibeault BJ, Pinsky B, Yanik AA. Mechanisms of Fano-resonant biosensing: Mechanical loading of plasmonic oscillators. Opt Commun 2020;469: 125780.
[49] Wang YM, Chen YX, Li XH, Lv SY, Hu JY, Zhang ZY, et al. Optical-intensity modulator with InSb nanosheets. Appl Mater Today 2020;21:100852.
[50] Gupta DN. Optical Second-Harmonic Generation of Terahertz Field from n-type InSb Semiconductors. Plasmonics 2021;16:419–24.
[51] Arlauskas A, Subačius's L, Krotkus A, Malevich VL. Terahertz emission from InSb illuminated by femtosecond laser pulses. J Phys D Appl Phys 2017;50:055101.
[52] Wang Q, Tang QY, Zhang DW, Wang ZF, Huang YS. Tunable terahertz spectral filter based on temperature controlled subwavelength InSb grating. Superlattices Microstruct 2014;75:955–61.
[53] Chen S, Fan F, Wang XH, Wu PF, Zhang H, Chang SJ. Terahertz isolator based on nonreciprocal magneto-metasurface. Opt Express 2015;23(2):1015–24.
[54] Qi LM, Yang ZQ, Lan F, Gao X, Shi ZJ. Properties of obliquely incident electromagnetic wave in one-dimensional magnetized plasma photonic crystals. Phys Plasmas 2010;17:042501.
[55] Trentini GV. Partially reflecting sheet arrays. IRE Trans Anntenas Propag 1956;4 (4):666–71.